Fe-N-C Electrocatalysts' Durability: Effects of Single Atoms' Mobility and Clustering

Kavita Kumar, Tristan Asset, Xiaoyan Li, Yuanchao Liu, Xingxu Yan, Yechuan Chen, Michel Mermoux, Xiaoqing Pan, Plamen Atanassov, Frédéric Maillard, et al.

Fe-N-C Electrocatalysts' Durability: Effects of Single Atoms' Mobility and Clustering

Kavita Kumar,[1,ξ] Tristan Asset,[2,ξ] Xiaoyan Li,[3] Yuanchao Liu,[2] Xingxu Yan,[4] Yechuan Chen,[2] Michel Mermoux,[1] Xiaoqing Pan,[4] Plamen Atanassov,[,2] Frédéric Maillard,[1] Laetitia Dubau[*,1]*

[1] Univ. Grenoble Alpes, Univ. Savoie Mont-Blanc, CNRS, Grenoble-INP ⊢, LEPMI, 38000 Grenoble, France

[2] Department of Chemical & Biomolecular Engineering, Nacional Fuel Cell Research Center (NFCRC), University of California, Irvine, CA 92697, USA

[3] Laboratoire de Physique des Solides CNRS, Université Paris Sud, 91405 Orsay, France

[4] Department of Materials Science & Engineering and Department of Physics & Astronomy, Irvine Materials Research Institute (IMRI), University of California Irvine, California 92697, USA

ᵻ Institute of Engineering and Management Univ. Grenoble Alpes

ξ These authors contributed equally to this work.

TABLE OF CONTENTS

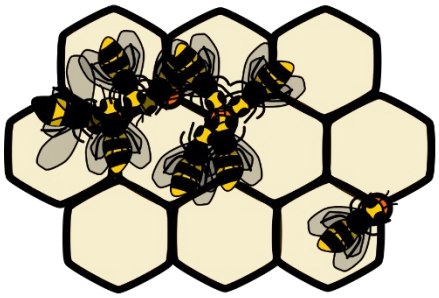

Bee cluster beeing inefficient for the oxygen reduction reaction

ABSTRACT

Atomically dispersed (or single atom) iron-nitrogen-carbon (Fe-N-C) catalysts are promising alternatives to platinum group metals (PGM) nanoparticles supported on dispersed carbon as a cathode material in proton exchange membrane fuel cells. Here, the degradation mechanism of Fe-N-C catalysts, synthesized by the sacrificial support method (SSM), was investigated by conducting accelerated stress tests under "load cycling" protocol (*i.e.* from 0.6 to 1.0 V *vs.* the reversible hydrogen electrode, RHE). Electrocatalyst activity towards the oxygen reduction reaction (ORR) was studied for a SSM-derived material, obtained by a single pyrolysis under 7% H_2 atmosphere (Fe-HT_1) and juxtaposed to that of a catalyst derived from the same sample, but subjugated to a second pyrolysis under 10% NH_3 (noted as Fe-HT_2). Several findings can be highlighted: (i) the second pyrolysis results in a skewing of the mesopores size toward higher diameter, along with an increase in iron content and N-pyridinic moieties, leading to a combined benefit in terms of ORR activity and selectivity; (ii) the morphological changes of these catalysts during ageing are drastically different depending on whether they were exposed

to a second pyrolysis as, for example, (iii) for Fe-HT_2, the formation of Fe-clusters was observed after the load cycling ageing protocol performed at T = 80°C, along to a partial corrosion of the amorphous domains. No clustering was observed at T = 60°C concomitantly with a higher ORR mass activity retention providing some guidelines to improve the stability of Fe-N-C materials.

KEYWORDS: Oxygen reduction reaction (ORR); Fe-N-C electrocatalysts; Atomically dispersed catalysts; Single atom mobility; Metallic Clustering.

INTRODUCTION

One of the challenges to overcome for the large-scale development of proton exchange membrane fuel cells (PEMFC) is the development of highly active and stable electrodes able to efficiently catalyze the oxygen reduction reaction (ORR). Among several platinum group metal (PGM)-free electrocatalysts for the ORR, the most promising candidates are based on iron (Fe) or cobalt (Co) ions coordinated with nitrogen (N) atoms, and embedded into a turbostratic or graphitic carbon (C) matrix (M-N-C catalysts)[1-2]. It is generally accepted that the transition metal species in M-N-C catalysts exist in two main types of species: (i) atomically dispersed moieties consisting of single metal ion coordinated to several N atoms, present as substitutional defects in the carbon matrix, M-N_xC_y sites, where *x* is usually 2, 3 or 4, and *y* denotes the number of carbon atoms in the second coordination sphere and (ii) metallic or inorganic transition metal-containing nanoparticles (carbides, nitrides, sulphides, etc., depending on precursors and synthesis protocol, often denoted with a “core-shell” nomenclature as Metal@NC) [3-4]. These nanoparticles often exhibit inexistent, or really low activity for the ORR in acidic environment, along with poor

stability [5]. It been shown in many studies, that optimal ORR activity is achieved for metal ions coordinated to four N atoms in the graphitic plane (FeN_4, FeN_3, FeN_{4+1}) or for those at the edges of two different graphitic sheets (FeN_{2+2}, N-Fe_{2+2}) [2, 6-11], thus giving the rise to the terms “in-plane” and “edge” atomically dispersed active sites. To achieve this structural arrangement, critical to withstand the high electrode potential, extreme low pH of the super-acidic Nafion electrolyte, and oxidizing environment of a PEMFC cathode, a mix of C, N, and transition metal (M = Fe, Co, Ni, *etc.*) precursors is pyrolysed at high temperature (the pyrolysis step provides the energy necessary to promote both N and metal atoms incorporation in the carbonaceous substrate, eventually forming the M-N_xC_y sites). The manifested catalytic activity of these active sites towards the ORR not only depends on their local coordination, but also on the type of porosity they are located in. For example, FeN_{2+2} sites are often found in micropores (*i.e.* pores < 2 nm), which suffer from (i) restricted (Knudsen) diffusion proceed of oxygen molecules, (ii) easy flooding during operation, (iii) imperfect impregnation by ionomer, thus resulting in a slow proton transport [12-13] .

Additionally, N atoms, incorporated in the carbonaceous matrices in pyridinic or pyrrolic coordination have also been reported to be ORR active [14-15]. However, in acidic environment, these sites (i) exhibit a depreciated turnover frequency (TOF) compared to the FeN_xC_y sites and (ii) do not support the 4-electron ORR process (*e.g.* pyrrolic-N, quaternary-N, graphitic-N only perform the $O_2 \rightarrow H_2O_2$ steps and N-pyridinic the $H_2O_2 \rightarrow H_2O$ step) [16]. Because pyrolysis is a key process for the formation of the active sites, some studies proposed the use of a second heat treatment under the same [17] or different gas conditions [18-19]. Such secondary pyrolysis usually follows a chemical etching or other "purification" processes, performed over the product of the first pyrolysis. In most cases, the second heat treatment (along with the preceding chemical treatments) revealed beneficial to the ORR activity [17-18, 20], and more particularly when the catalysts were re-pyrolysed under ammonia (NH_3) atmosphere [9, 21]. Specifically, Koslowski *et al.* evidenced that a second pyrolysis under NH_3 atmosphere resulted in a 2 – 3 fold increase in ORR mass activity *vs.* a N_2 second pyrolysis under identical conditions for Fe and Co-porphyrins. They also noted a notably higher content in metallic and nitrogen moieties (6.7 at. % *vs.* 4.6 at. % for the nitrogen moieties) when performing a NH_3 second pyrolysis over

a N_2 second pyrolysis [19]. However, the long-term benefits of such second pyrolysis in the conditions of the application remain underexplored and, as such, are the focus of this study.

In this work, two different Fe-N-C electrocatalysts were synthesized by the sacrificial support method (SSM) [22-24] using a silica template, nicarbazin and Fe-containing precursors. Both materials were first pyrolysed at T = 975°C in a gas mix consisting of N_2 and H_2 with 93:7 ratio, but only one was exposed to a second pyrolysis at T = 950°C in a gas mix of N_2 and NH_3 with 90:10 ratio. The second pyrolysis was performed after removal of the silica template from the materials obtained in the first pyrolysis by leaching in HF. A combination of transmission electron microscopy (TEM), high-angle annular dark-field scanning transmission electron microscopy (HAADF-STEM), Raman spectroscopy, X-ray diffraction (XRD), Brunauer-Emmet-Teller (BET) nitrogen gas chemisorption, and X-ray photoelectron (XPS) techniques was used to provide relevant information about the physical and chemical properties of the two different catalysts in their fresh and aged state. The positive effect of a second heat treatment under NH_3 atmosphere towards the ORR

is confirmed. However, accelerated stress test (AST) protocols on this material reveal that single Fe atoms agglomerate and form clusters, but not nanoparticles, after the load-cycling AST in Ar-atmosphere.

RESULTS AND DISCUSSION

The effect on the second pyrolysis step on the catalyst physical and chemical properties

The different Fe-N-C catalysts were prepared using the SSM, and are referred to as Fe-HT_1 and Fe-HT_2 for a single heat treatment and two heat treatment steps, respectively. The first pyrolysis was performed at T = 975°C (for 45 min) in N_2:H_2 gas mix 93:7, and the second pyrolysis at T = 950°C (for 30 min, leading to a total pyrolysis time of 75 min) in N_2:NH_3 gas mix 90:10. **Figure 1a** and **1b** show transmission electron microscopy (TEM) images of Fe-HT_1 and Fe-HT_2, respectively. Similar morphology was observed for both electrocatalysts, which is stacked graphitic sheets in which the carbon phase was highly structured. Energy dispersive X-ray (X-EDS) spectroscopy analyses revealed that the Fe content was 0.08 at. % after the first pyrolysis step (Fe-HT_1 sample) and increased up to 0.14 at. % after the second pyrolysis, in agreement with former findings of Ferrandon *et al.* on a polyaniline iron carbon material [17]. We rationalized this by considering production of hydrogen cyanide (HCN) from the reaction between C and NH_3 [25]. This reaction nevertheless did not result in aggregation of Fe atoms as confirmed by HAADF-STEM

(see following sections) and XRD (see **Figure S1a**). Our finding is in line with former extended X-ray absorption fine structure (EXAFS) [26] and Mössbauer spectroscopy [27] results, indicating that, at a bulk level, this SSM process results in atomically dispersed M-N_xC_y active sites.

The evolution of carbon matrix's structural parameters derived from XRD and Raman spectroscopy before and after the second pyrolysis is displayed in **Figure 1c** (spectra and diffraction patterns are shown in **Figure S1a-b**). While the interlayer spacing (d_{002}) remains unchanged, the crystallite size in the graphene plane (L_a) or perpendicular (L_c) to the graphene sheets slightly increases after the second pyrolysis under NH_3. Although this increase remains within the experimental error, it can be assumed that, in average, Fe-HT_2 catalysts are more graphitic than Fe-HT_1. This is induced by the pyrolysis under NH_3. Indeed, the later results in a degradation of exposed carbon through the formation of HCN from C and NH_3, with far greater kinetics for the amorphous carbon *vs.* the graphitized carbon [25]. However, based on the changes in iron bulk content from X-EDS (see Figure 1), it can be inferred that the carbon etching process was structure-insensitive, hence

explaining why the iron content increased from 0.08 wt. % to 0.14 wt. % during the NH3 pyrolysis without significant changes in the degree of graphitization. Along with this mild change, the specific surface area of the Fe-HT_2 catalyst is slightly superior to that of Fe-HT_1 (**Figure 1d**), as shown by pore size distribution derived from the Brunauer-Emmett-Teller (BET) nitrogen cryo-adsorption isotherms analysis (**Figure S1c**).

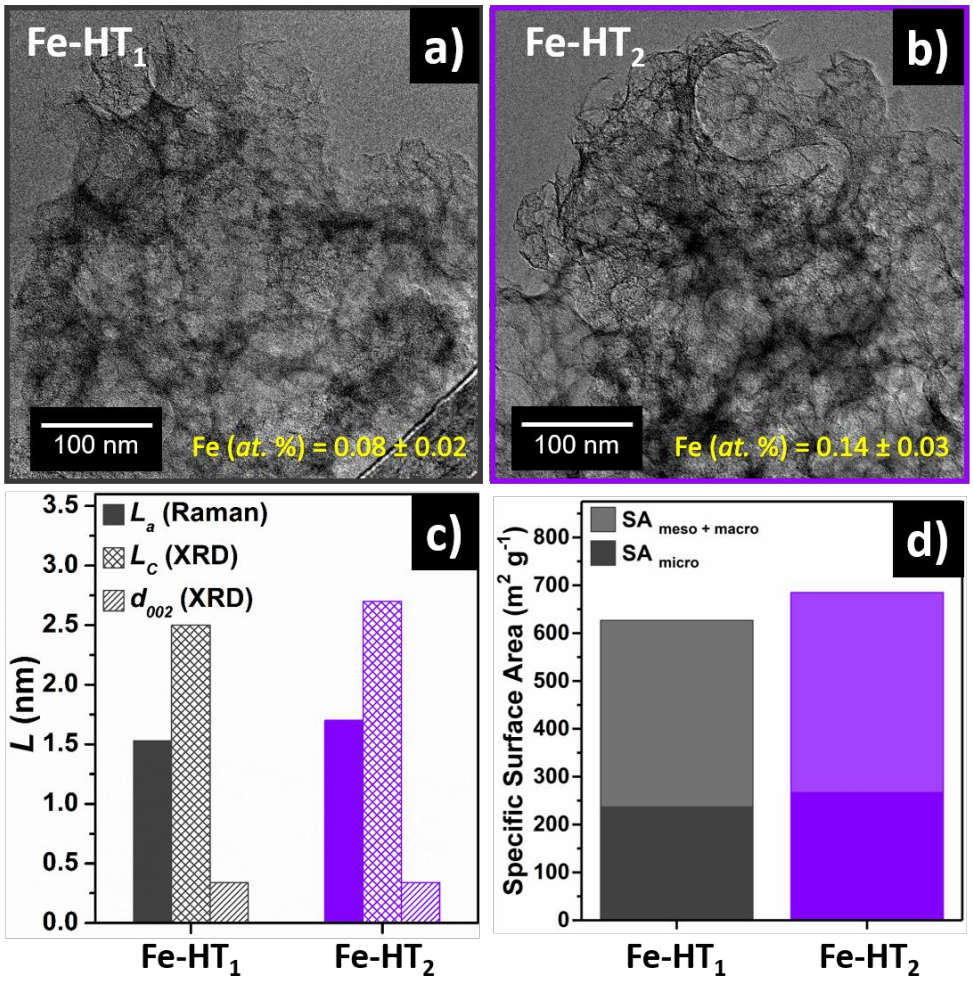

Figure 1. Physical characterizations of the two Fe-N-C fresh catalysts used in this study: (a, b) Transmission electron microscopy images. The iron content was estimated as the (Fe/(Fe + C)) ratio evaluated using energy dispersive X-ray spectroscopy. The error values were obtained from at least six independent measurements in different zones. (c) Carbon crystallite size in the graphene plane and perpendicular to the graphene sheets and interlayer spacing (L_a, L_c and d_{002}, respectively). (d) Specific surface area estimated from BET analysis.

To evaluate the porosity change in second pyrolysis (micro- and mesopores), pore size distribution by NLDFT model (Non-Local Density Functional Theory) was used (**Figure S1d-e**). Significant changes are observed in the pore size distribution, *i.e.* the second heat treatment leads to an overall shift of the mesopores volume and surface toward larger pore width. This result can be assigned to higher meso- and macroporous areas for the Fe-HT_2 material, as a result of the chemical etching of NH_3 on carbon surface. In contrast to MOF-derived catalyst [28], in which the second pyrolysis step under NH_3 results in an increase of both the specific surface area (2.3-fold) and the microporosity (+ 10 % in Ref. [28], although the microporosity content can increase up to + 60 % as a function of the synthesis conditions [29]) of the materials, here, the specific surface area are little affected

by the second pyrolysis step (**Figure 1d)**. The increase of mesoporosity after the second pyrolysis is likely to result in a higher proportion of in-plane Fe-N_4 sites, contrary to other families of catalysts [2, 29-33], wherein the majority of the FeN_x moieties is located in the micropore structure. This assumption arises from the fact that mesopores often exhibit exposed graphitic planes (which host Fe-N_4, Fe-N_3 and Fe-N_{4+1} moieties) [8], whereas the Fe-N_{2+2} and N-Fe-N_{2+2} moieties are found on graphitic carbon edges, which are, in turn, present in micropores.

XPS analysis provided chemical insights into the impact of the second heat treatment under NH_3 atmosphere on the near-surface layers of the material (**Figure 2**). Among the notable features (i) the near-surface relative atomic content in C increased after the second pyrolysis, (ii) the content in C sp^3 slightly increased (see **Table S1** in Supporting Information); (iii) the N-pyridinic content dramatically increased after the second pyrolysis (*i.e.* from 0.70 at. % to 0.84 at. %, see **Table S2** in Supporting Information), whereas the abundancy of the other moieties (N-pyrrolic, N_{gr}/N^+, Fe-N_x) decreased. The decrease in Fe-N_x (0.59 at. % to 0.46 at. %) is explained by the contribution of the amine peak at 399.9

eV to its peak [34], and the assumption that the latter is the one mainly impacted by the NH_3 pyrolysis; (iv) a marked decrease in oxygen content was observed (*i.e.* 4.4 and 3.0 at. % for Fe-HT_1 and for Fe-HT_2, respectively), the latter being induced by the reductive nature of the NH_3, the preferential NH_3-induced gasification of the amorphous, oxygen rich domain of the carbon (HCN formation) and the fact that pyrolysis often leads to the desorption of the oxygenated groups. The increase in C sp^3 corroborates with the increase in meso + macroporosities observed in **Figure 1d**, the latter being constituted of more structurally ordered, graphitic, carbon. According to the previous research [14], N-H moieties contribute to the partial electrocatalytic reduction of oxygen molecules to peroxide while pyridinic N moieties can reduce H_2O_2 to water. Hence the more balanced ratio between N-H and pyridinic N after ammonia heat treatment (decrease from 34.6 % / 19.5 % to 31.2 % / 25.5 %) will result in a decent decrease of peroxide yielding. In conclusion, although the overall specific surface of the electrocatalyst exhibit small differences between Fe-HT_1 & Fe-HT_2, the latter appears as more graphitic, with a pore size distribution skewed toward higher widths, a larger Fe content, and a more balanced distribution of nitrogen-containing moieties.

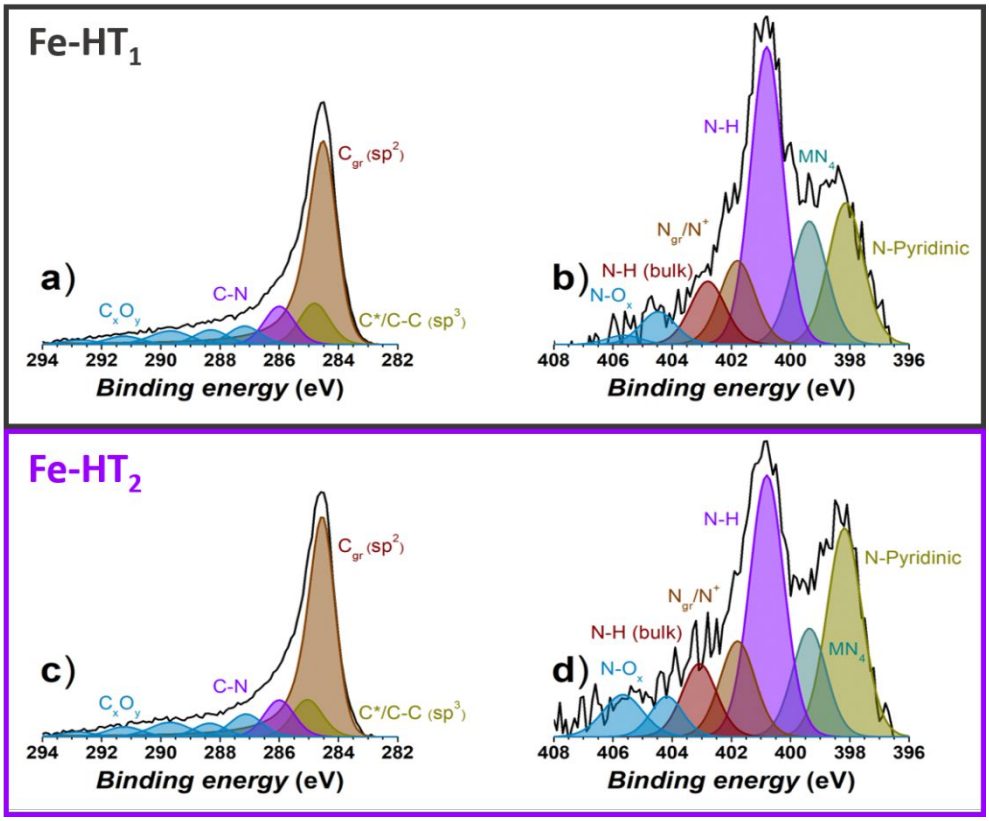

Figure 2. High resolution X-ray photoelectron spectra in the (a, c) C1s and (b, d) N1s region, for Fe-N-C electrocatalysts after (a, b) a pyrolysis at T = 975 °C in 7 % H_2, (c, d) the first pyrolysis and a second at T = 950 °C in 10 % NH_3.

The effect on the second pyrolysis step on electrocatalytic activity

The second pyrolysis under NH_3 atmosphere also led to marked increase of the ORR mass activity (1.8-fold enhancement, see **Figure 3a**) as expected from previous works [17-18], but did not affect the pseudocapacitance of the catalyst (**Figure 3b**), supporting the

previously results obtained from bulk analysis (XRD and Raman). The NH_3 treatment also modified the selectivity of the ORR, since the results from Rotating Ring-Disk Electrode (RRDE) measurements (**Figure S2**) revealed that at E = 0.6 V *vs.* RHE, 79% and 18% of H_2O_2 is released from the catalytic layer for Fe-HT_1 and Fe-HT_2, respectively (**Figure 3c**). The huge decrease of peroxide yielding probably comes from the balanced N moieties distribution (decrease of N-H and increase of pyridinic N) after ammonia heat treatment, which is consistent with the change of N 1s from the XPS results, as described previously. Our results thus imply that the NH_3 treatment on SSM materials (i) revealed new ORR active sites (initially buried into the disordered carbon phase/micropores) in the mesoporous surface of the Fe-HT_2 material, which are different from Fe-HT_1 and able to perform the direct reduction of the O_2 via 4 e^- pathway or; (ii) integrated new nitrogen species into the carbon matrix allowing an ORR mechanism *via* a 2+2 e^- process.

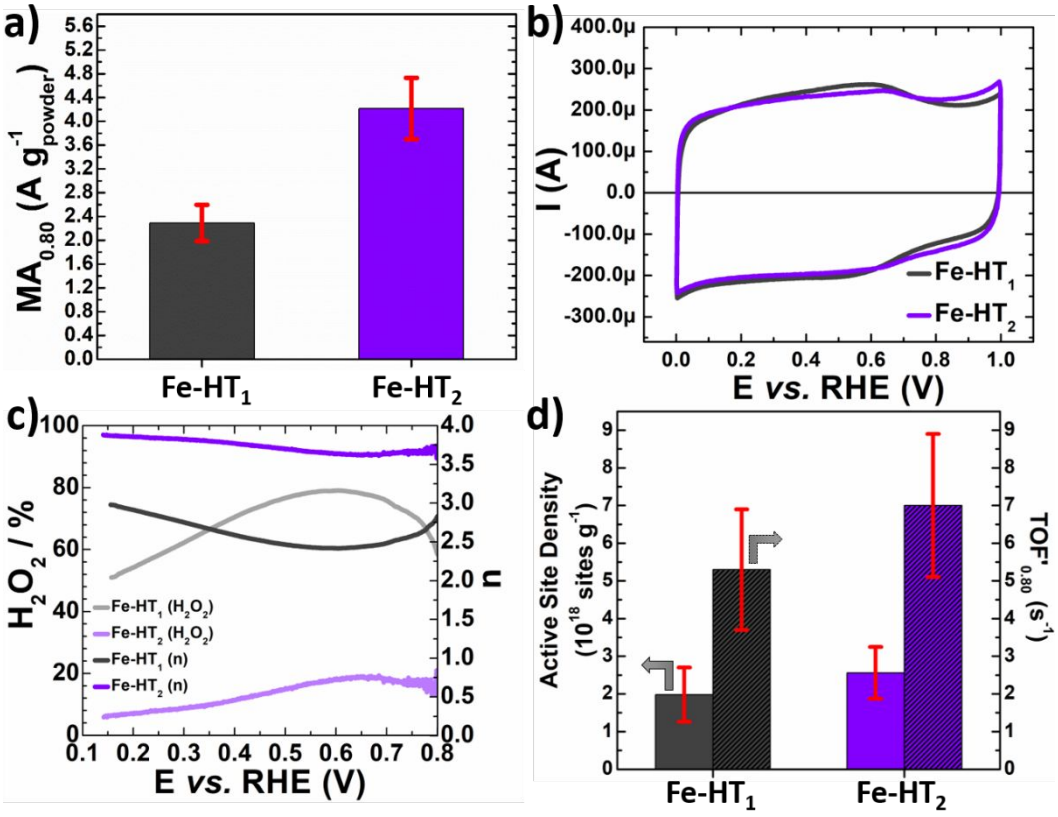

Figure 3. (a) Oxygen reduction reaction mass activities of fresh Fe-N-C materials measured at E = 0.80 V *vs.* RHE. The error bars are the standard deviation obtained from at least eight different measurements. The ORR measurements were performed in O_2-saturated 0.1 M H_2SO_4 electrolyte, recorded at 1600 rpm and at v = 5 mVs^{-1}. The catalyst loading was 800 μg cm^{-2}. (b) Cyclic voltammograms of Fe-N-C catalysts recorded at v = 10 mVs^{-1} in Ar-saturated 0.1 M H_2SO_4 electrolyte. (c) H_2O_2 yield produced during the ORR and number of electrons transferred during the ORR (n) for Fe-based catalysts. The catalyst loading was 100 μg cm^{-2}. (d) Active site density and turnover frequency (TOF') values measured at E = 0.80 V *vs.* RHE using a chemisorption method with nitrite ions [35]. The error bars are the standard deviation obtained from at least two different measurements. The SD values were determined by using the *in situ* nitrite method,

performed in 0.5 M acetate buffer at *pH* = 5.2 and at *T* = 25°C, and the TOF' values were calculated from the ratio between the MA obtained at *pH* = 1 and the SD measured at *pH* = 5.2. The catalyst loading was 300 μg cm^{-2}.

To gain insights into these two hypothesis, the active site density (SD) and the turnover frequency were evaluated using the *in situ* nitrite adsorption/reduction electrochemical method first introduced by Malko *et al.* [35]. Whereas an increase in the SD value would validate the first hypothesis that the second pyrolysis step revealed new active sites initially hidden in the bulk of the carbon matrix, an increase of the TOF values for Fe-HT_2 would confirm the assumption that nitrogen-rich environment favors a 2+2 e^- pathway for ORR (a 3.2-fold increase of the TOF value after NH_3 pyrolysis has been reported by Kramm *et al.* [25]). The *in situ* nitrite adsorption/reduction method relies on chemisorption of nitrite (NO_2^-) ions onto the Fe^{2+} ions followed by reductive stripping of NO into NH_3 *via* 5-electron process, the charge of which leads to the site density (SD) and, by dividing the SD by the decrease in ORR activity before/after nitrite poisoning, to the TOF (electrons $site^{-1}$ s^{-1}) values. The cyclic voltammograms, the ORR polarization curves and the Tafel plots before, during and after nitrite adsorption are shown in **Figure S3**. Surprisingly,

although after a NH_3 treatment, a 1.8-fold increase of the MA of the material was assessed (*i.e. ca.* 2.29 A g^{-1} for Fe-HT_1 *vs. ca.* 4.21 A g^{-1} for Fe-HT_2, see **Figure 3a**), this result did not translate into a corresponding increase of the SD values (*i.e. ca.* 2.0 10^{18} g^{-1} for Fe-HT_1 *vs. ca.* 2.6 10^{18} g^{-1} for Fe-HT_2, see **Figure 3d**). Even more striking, a 2.1-fold decrease of the TOF number was measured for the Fe-HT_2 catalyst (*i.e. ca.* 14.5 s^{-1} for Fe-HT_1 *vs. ca.* 6.7 s^{-1} for Fe-HT_2, see **Table S3** in the supporting information), hence suggesting that the quantification with the nitrite adsorption/reduction method is limited when applied to catalysts pyrolysed under NH_3. In a recent article comparing two different methods of active sites quantification for Fe-N-C catalysts, [36] several issues related to the *in situ* nitrite method were raised by the authors: (i) the fact that the measurement needs to be performed at *pH* = 5.2, which is less acidic than the standard operative conditions of a PEMFC device [36], (ii) even if most of the ORR activity (70 %) is lost during the nitrite adsorption, a non-negligible ORR activity remains, testifying the presence of different types of FeN_x sites in the materials and suggesting that nitrite anions could not be adsorbed into all exposed sites due to their very high chemical specificity. Thus, we believe that this method cannot be applied for all iron-based catalysts, in particular for

those treated by a NH_3-based second pyrolysis, as the chemisorption of nitrite might be impacted by the basicity of N-groups. This hypothesis is supported by the literature showing that the NH_3 treatment strongly increases the basicity of the N-C matrix [28, 31, 37], and could consequently reduce the interaction strength between the nitrite ions and the Fe-based moieties due to the electron-donating properties of the neighboring nitrogen groups. To further explore this finding, we decided to assess the TOF (here referred as TOF') by using the site density measured by the nitride adsorption method at *pH* = 5.2 and the mass activity measured at *pH* = 1 (**Figure 3d**). These new TOF' values are more consistent with our previously findings, since after the second heat treatment the TOF' value increased 1.3-fold. In summary, the second pyrolysis under NH_3 atmosphere greatly increases the ORR activity and selectivity of the catalyst but limits the utilization of the nitrite method to quantify the active site density and their turnover frequency.

The effect on the second pyrolysis step on the catalyst durability

To gain insights into the effect of a second pyrolysis under NH_3 atmosphere on the electrocatalyst stability, a load-cycling (LC) protocol composed of 10,000 square cycles

between 0.6 and 1.0 V *vs*. RHE (holding time 3 s at each potential) was performed at T = 80°C in Ar-saturated acidic electrolyte. The normalized ORR mass activity (MA) measured at E = 0.80 V *vs.* RHE of Fe-HT_1 and Fe-HT_2 before and after the AST are shown in **Figure 4a**. The MA values were extracted from the ORR polarization curves after correction of the Ohmic drop, the oxygen diffusion in the solution and the pseudocapacitive current (brutto ORR polarization and cyclic voltammograms may be found in **Figure S4**). The ORR mass activities dropped by 56 % and 44 % after LC for Fe-HT_1 and Fe-HT_2, respectively. Unlike to what was observed on metal-organic framework (MOF)-derived catalysts [28, 31, 38], the NH_3-treatment appears to improve the stability of the material.

In order to explain the massive ORR activity, drop after the ASTs, the normalized ratios between Fe and C content, estimated by local X-EDS analyses, are shown in **Figure 4b**. The local Fe content decreased after the LC protocol for both catalysts, but this cannot account for the massive MA loss after the AST. Indeed, in our previous work [5] addressing the stability of Fe-N-C catalysts derived from MOFs, where most of the ORR active sites were located in the micropores of the material, we showed a correlation between the

normalized Fe content and the MA losses after the LC ageing protocol. In this manuscript, *i.e.* for Fe-N-C catalysts synthesized by the SSM, the ORR active sites are mainly found in the mesopores. Moreover, in an internal comparative study on MOF-derived catalysts, we also noticed different stability trends, suggesting that materials with L_a values less than 2.5 nm do not respect the linear correlation between the Fe loss (evaluated by X-EDS analysis) and the MA loss after LC protocol. Confronting the results of the same AST on two different families of catalysts, we thus came to the conclusion that the degradation mechanisms of M-N-C catalysts are dependent on the active sites localization within the catalyst structure and the degree of graphitization of the carbon matrix.

During the LC protocol, the COR (carbon oxidation reaction) mainly affected the disordered carbon domains on the Fe-HT_2 material (**Figure 4d**). This is evidenced by a sharpening of the Raman features on Fe-HT_2 which, surprisingly, was not observed on Fe-HT_1 (see **Figure 3c** and **3d**) In particular, the D_1 (1350cm^{-1}), G (1580 cm^{-1}) and D_3 (1495 cm^{-1}) bands narrowed for the Fe-HT_2 catalyst. Moreover, in the second-order region of the spectra, three different bands appeared after the AST for Fe-HT_2 catalyst. These

are located at 2710, 2920 and 3240 cm^{-1}, that can be attributed to a combination and overtones of *G*, D_1 and *D'* bands [39]. This result suggests that disordered carbon domains were preferentially corroded during the LC ageing protocol on Fe-HT_2, leaving behind the most graphitic domains. In contrast, the proportion between structurally-ordered (graphitic) and structurally-disordered domains remained nearly identical on Fe-HT_1 during the LC protocol. Such discrepancy between the two electrocatalysts might arise from the increased basicity of the carbon surface following the (second) NH_3 pyrolysis, which leads to the carbon amorphous domains being more sensitive to electrochemical corrosion.

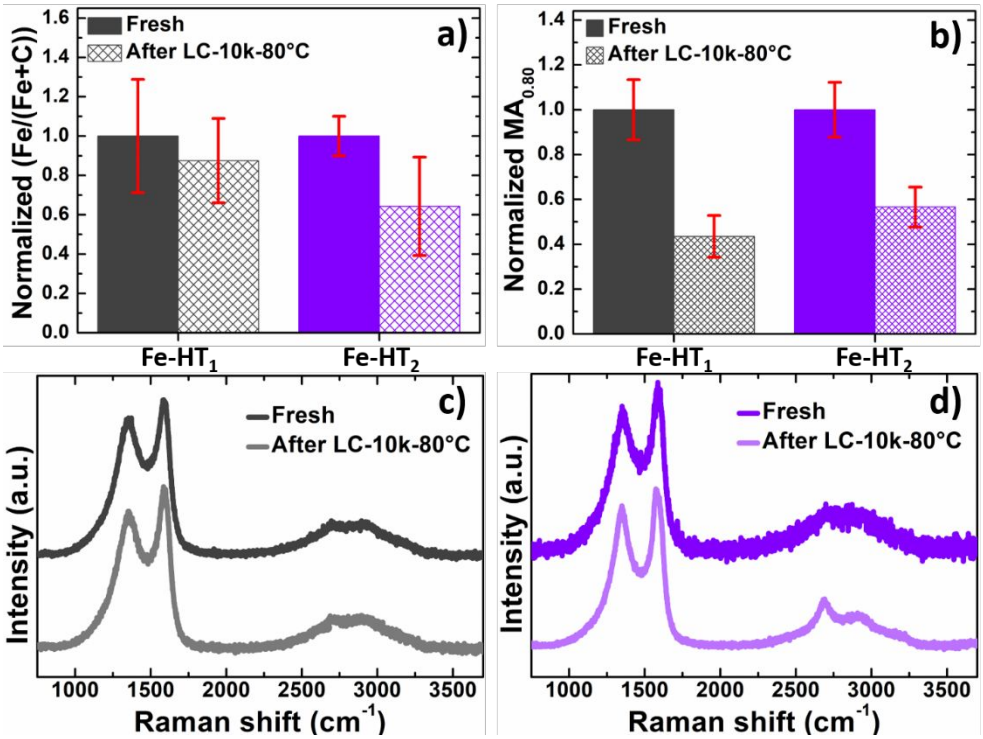

Figure 4. (a) Normalized ORR mass activity at E = 0.8 V *vs.* RHE of Fe-N-C catalysts determined before / after 10,000 load-cycles (LC) at T = 80°C. The ORR activities were obtained using a rotating disk electrode in O_2-saturated 0.1 M H_2SO_4 (1600 rpm, T = 25°C, v = 5 mV s^{-1}) using a catalyst loading of 800 µg cm^{-2}. The error bars are the standard deviation obtained from at least two different measurements. (b) Normalized Fe content in the Fe-N-C catalysts before and after ASTs. The error bars were obtained from at least six independent measurements in different zones. (c) Raman spectrum of Fe-HT_1 before and after ASTs performed at 80°C. (d) Raman spectrum of Fe-HT_2 obtained on the fresh and aged catalyst.

In order to unravel the consequences of the second pyrolysis step on the degradation mechanism occurring during the LC protocol, the Cs-corrected atom-resolved HAADF-STEM was performed for Fe-HT_1 and Fe-HT_2 materials (see **Figure 5**).

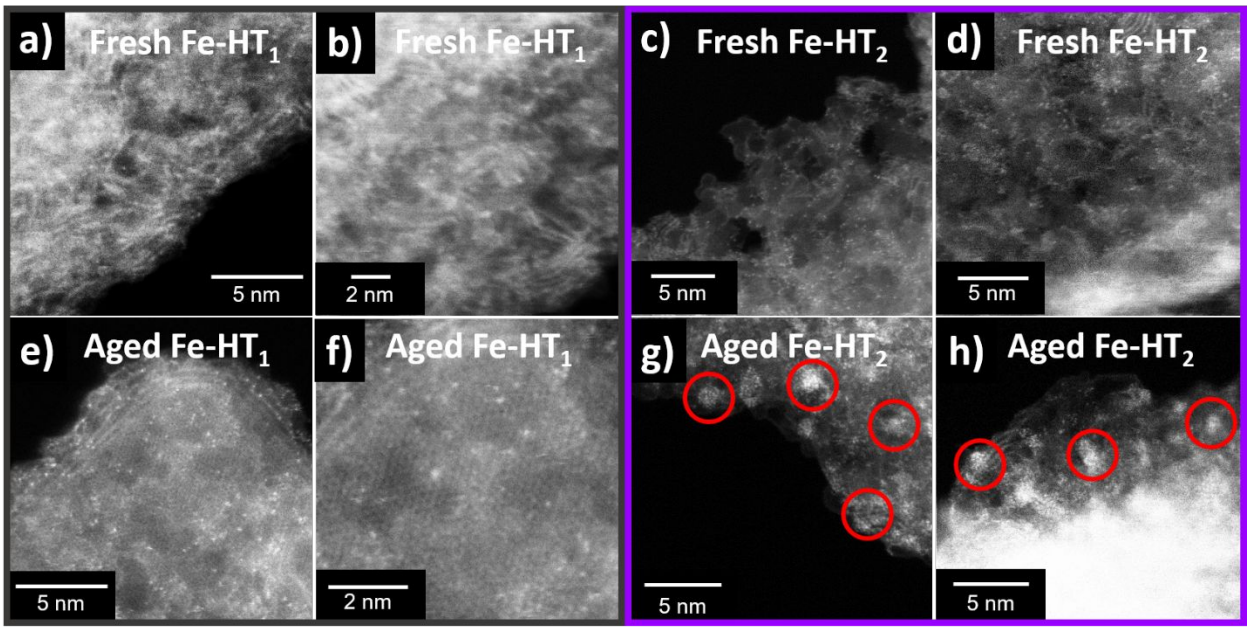

Figure 5. HAADF-STEM images of the Fe-HT_1 and Fe-HT_2 electrocatalysts (a-d) before and (e-h) after 10,000 load-cycles between 0.6 and 1.0 V *vs.* RHE in Ar-saturated 0.1 M H_2SO_4 thermostated at T = 80°C. The formation of clusters is underlined by the red circles.

While the fresh catalysts feature exclusively atomically dispersed Fe atoms grafted onto a carbon substrate (**Figure 5a-b** and **5c-d**), only the Fe-HT_2 aged material (following the

load-cycle protocol) exhibits some small Fe nanoclusters after AST (**Figure 5g-h**), in line with recent results of Wu *et al.* [40-41]. Bridging electron microscopy and Raman spectroscopy results, we thus conclude that Fe nanocluster formation occurs concomitantly to the carbon corrosion during the LC protocol (which was shown to take place at $E > 0.9$ *vs.* RHE [42]). We argue that the cluster formation is induced by a cleaving/breaking of the Fe-N bonds at high potentials, thus promoting the displacement of Fe atoms onto the basal planes or between the first and second graphene planes. Eventually, these Fe atoms anchor in another region of the carbon matrix or agglomerate, the required energy being brought by the high temperature encountered during the AST ($T = 80$°C). The fact that this phenomena is not observed on the Fe-HT_1 indicates that it is induced by the (second) NH_3-pyrolysis and, thus, the change in surface chemistry/basicity induced by the latter.

To gain further insights into this unprecedented mobility of Fe atoms, HAADF-STEM imaging was used to investigate the identical locations (**Figure 6**) for the Fe-HT_2 material before after the load-cycling protocol. Note that the load-cycling protocol was performed

at T = 60 °C in Ar-saturated electrolyte (LC-10k-Ar-60°C) to prevent corrosion of the carbon membrane of the TEM grid. However, this temperature of 60°C does not prevent the degradation mechanisms from producing but it slows them down [42-44] as shown by our HAADF-STEM measurements on the thin regions of the N-doped C particles. For example, the clogging of a mesopore (see Zone 1, **Figure 6a** and **Figure 6b**) as well as a densification of the N-doped C matrix (see Zone 2, **Figure 6c** and **Figure 6d**) are worth noting, both phenomena being typical of the COR. The second remarkable result is that no iron atoms clustering was observed. Accordingly, the material stability was increased (the MA dropped only by 34 % after AST operated at T = 60 °C compared to a 44 % drop after the same AST performed at T = 80°C, see **Table S3**).

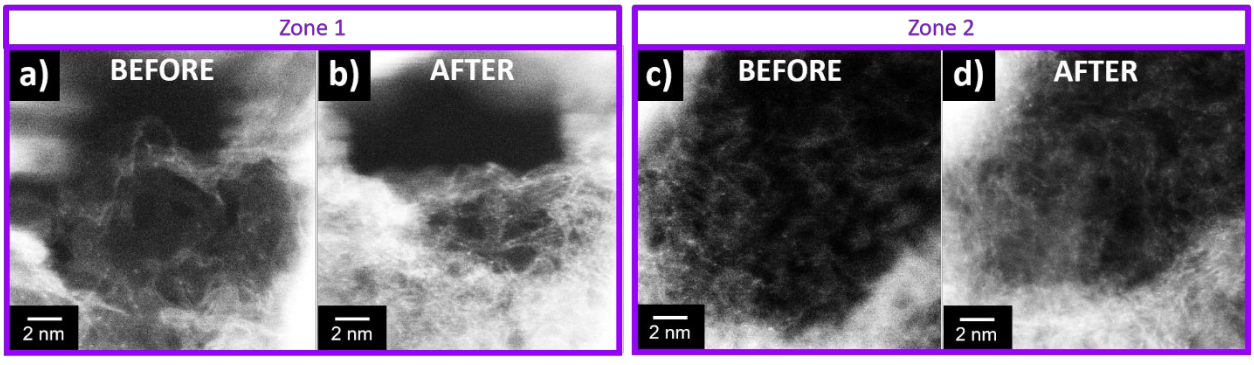

Figure 6. HAADF-STEM images of Fe-HT_2 catalyst before and after 10,000 potential cycles between 0.6 and 1.0 V *vs*. RHE (3s at each potential, 'load-cycling' protocol) in Ar-saturated 0.1 M H_2SO_4 thermostated at T = 60°C. Images (a-b) and (c-d) are referred to the zone 1 and zone 2, respectively.

The nitrite adsorption/reduction method was performed before and after the different AST of Fe-HT_2 catalyst to observe the evolution of the SD and the TOF values (see **Table S3**). Although this method was questioned in the previous section, we believe that a qualitative comparison of the values obtained on the same material is relevant. Interestingly, the SD value increased after LC-10k-Ar-80°C (from 2.6 to 3.1 10^{18} g^{-1}), while it decreased after LC-10k-Ar-60°C (from 2.6 to 2.1 10^{18} g^{-1}) corroborating the effect of the temperature on the formation of iron clusters. Having in mind that the MA decay is more pronounced after the ageing test at 80°C, it seems that the iron clusters exhibit no or at least very low ORR activity. In our previous work [44], we also noticed an increase of the SD value for a MOF-derived material after ageing. The effect of O_2 atmosphere on the stability of Fe-N-C catalysts was evaluated, and iron oxide nanoparticles grafted into the N-C matrix of the Fe-N-C catalysts were observed after load-cycling protocol in O_2-saturated acidic electrolyte at T = 80°C. After different tests using commercial iron oxide

particles, it was concluded that the nitrite anion, used for the nitrite adsorption method, can also probe iron nanoparticles. Such conclusions might extend to iron nanoclusters, as observed for the LC-10k-Ar-80°C and thus, coupled with a different nitrite adsorption process on clusters/nanoparticles *vs*. atomically dispersed iron, explain the SD increase. Note also that the second TOF values (TOF') estimated using the MA determined at pH = 1 and the SD measured at pH = 5.2 appeared more relevant for this study, since the TOF' values decrease after the AST for the Fe-HT_2 catalyst (see **Table S3**).

To determine whether the formation of iron oxide nanoparticles also takes place on electrocatalysts synthesized by the SSM method, we investigated the Fe-HT_2 stability in O_2-saturated electrolyte at T = 80°C. After LC-10k-O_2-80°C, the MA activity of the Fe-HT_2 dropped by 79 % (see **Table S3**) and iron nanoparticles were observed in the TEM images (see **Figure S6**), the latter being likely responsible for the drop in MA, along with eventual Fe reaction with peroxide species to form radical oxygen species, *via* the Fenton reaction.

CONCLUSIONS

In this work, we investigated the stability of Fe-N-C electrocatalysts synthesized by the sacrificial support method, along with the role of a second pyrolysis, performed under N_2 - NH_3 gas mix (90:10) on their stability during accelerated stress tests mimicking proton exchange membrane fuel cell cathode conditions, *i.e.* load-cycle (LC, 0.6 – 1.0 V *vs.* RHE). Physico-chemical characterization revealed only slight changes between the catalysis after first pyrolysis (Fe-HT_1 pyrolysed under N_2 - H_2 gas mix 93:7) and the one subjugated to a second pyrolysis (Fe-HT_2 – with two pyrolysis steps performed consequentially) electrocatalysts, namely a skewing of the pore width toward higher diameter, a slight increase in graphitization and a higher content of C sp^3 and N-pyridinic. However, the treatment in ammonia containing atmosphere greatly increased both the ORR activity and the selectivity of the Fe-HT_2 material, along with affecting its degradation mechanism. The formation of Fe-clusters was observed during a load cycling ageing at T = 80°C for Fe-HT_2, but not for a catalyst obtained in single pyrolysis step (Fe-HT_1). The formation of iron clusters also depends on the temperature at which the ageing test are performed, *i.e.* at

T = 60°C, no cluster formation was observed on the Fe-HT_2 resulting in a better mass activity retention. One could hypothesize that the material after second pyrolysis offers different mechanisms for atomically dispersed transition metal mobility and restructuring. Those mechanisms may include higher levels of surface mobility and possible transformations between Fe-N_x-C_y edge and in-plane sites, ultimately leading to apparently 2D cluster formations. Elevated operating temperature of T = 80°C increases the PEMFC initial performance, yet it increases the rate of the main degradation mechanism as it leads to a display of new degradation mechanisms which ultimately may result in lower level of durability. Therefore, applications of current generation PGM-free catalysts of M-N-C type might still be limited to devices operating at moderate temperature (*e.g.* portable PEMFCs, AEMFCs or metal-air batteries), at this developmental stage.

MATERIAL AND METHODS

Catalysts

To prepare the Fe-N-C materials using the SSM method, a silica template is used, consisting of home-made Stöber spheres (1 g) + LM-150 (Cab-O-Sil®, 2.5 g) + OX-50 (Evonik®, 2.5 g) both product of Cabot Corp., and used "as received". The iron precursor is $Fe(NO_3)_{3*}9H_2O$ (Sigma Aldrich, 1.2 g) and the nitrogen-carbon precursor – nicarbazin, a charge transfers organic salt (12.5 g, Sigma Aldrich). The solid precursors were first mixed, then, distilled water was added in the mix, forming a viscous solution (slurry). The solution was stirred overnight at 45°C to obtain a near-dried mixture (paste), which was then fully dried in an oven at 40°C. This "wet impregnation" step was followed by grinding and ball-milling for 30 min at 45 Hz (sometimes refereed as "mechanochemical step"), followed by the *first pyrolysis* under gas mix containing 7% H_2 and 93% N_2. The *first pyrolysis* was performed as follows: (i) insertion of the catalyst at 525°C, followed by (ii) two temperature increases: from 525°C to 900°C (with duration of 12 min) and from 900°C to 975°C (with duration of 8 min) – "two-step ramp"; (iii) the temperature was then

maintained at 975°C (noted as “pyrolysis temperature”) for 45 min (referred to as “pyrolysis time”) and allowed to cool down to room temperature under the same reductive gas flow (7% H_2 + 93% N_2), while the tube is being stored out of the furnace (“air cooling” process). An HF:H_2O 2:1 leaching was then performed for 96 h, before washing with DI water and neutralization. This sample will then be labeled as Fe-HT_1 and referred to as “single” or “first pyrolysis” catalyst. A fraction of the same catalysts batch will then be subjugated to a *second pyrolysis* to form the sample Fe-HT_2. To achieve that, the catalyst after first pyrolysis and leaching (Fe-HT_1) was dried, ball-milled for a second time for 30 min at 45 Hz and pyrolysed for a second time for a duration of 30 min at 950°C. This second pyrolysis is performed under different atmosphere consisting of 90% N_2 and 10% NH_3 gas supplied as a mix. After the second pyrolysis, the catalysts were ball-milled one last time for 30 min at 45 Hz and recorded as Fe-HT_2.

Electrochemical Characterizations

Homogenous catalytic inks were prepared by mixing 10 mg of the electrocatalyst powder, 50 µL of a Nafion® suspension (5 wt. % in *n*-propanol), 854 µL of isopropanol, and 372 µL ultrapure water (Millipore, 18.2 MΩ cm at T = 20 °C, total organic compounds < 3 ppb). An aliquot of this ink was then deposited onto the working electrode, a glassy carbon disk of 5 mm diameter. Then, the deposit was dried under air using a heat gun in order to evaporate the Nafion® solvents, isopropanol and the water. The catalyst loading was 800, 100 and 300 μg_{powder} cm^{-2} for the electrochemical characterizations / ASTs, RRDE and the electrochemical quantification of the active sites, respectively.

All electrochemical measurements were carried out using a bi-potentiostat (Autolab PGSTAT302N) operated with NOVA 2.0 software. The totality of the glassware used in this work was cleaned using a H_2SO_4/H_2O_2 (50 % v/v) solution before use. We used two different four-electrode electrochemical cells: one for the characterization, at T = 25°C and another for the ASTs, at T = 80°C or T = 60°C. A carbon plate and a reversible hydrogen electrode (RHE, Hydroflex, Gaskatel GmbH) were used as counter-electrode and reference electrode, respectively.

The electrochemical experiments were carried out using a rotating disk electrode. For each sample, 50 cyclic voltammograms (CVs) were first recorded between 0.1 and 1.0 V *vs*. RHE at ν = 100 mV s^{-1} in Ar-saturated 0.1 M H_2SO_4 electrolyte. Subsequently, 3 CVs were recorded at ν = 10 mV s^{-1} to obtain the electrochemical signature of Fe-N-C samples followed by 1 CV at ν = 5 mV s^{-1} to correct ORR polarization curves from the pseudocapacitive current. Finally, the ORR polarizations curves were recorded at T = 25°C, at 1600 rpm, in O_2-saturated acidic electrode between 0.0 and 1.0 V *vs*. RHE before and after 10,000 AST cycles.

The RRDE experiments were performed in a home-made three electrode cell, using identical cleaning procedure than listed above, a carbon rod as the counter electrode and a reversible hydrogen electrode (RHE, Hydroflex, Gaskatel GmbH) as the reference electrode, the working electrode being a Pine Instrument RRDE with a glassy carbon disk surface of 5.6 mm diameter. After an activation procedure identical to the one described above, single CV were obtained in N_2-saturated 0.1 M H_2SO_4 for the ring and the disk at

2 mV s^{-1} from 0.1 to 1.05 V *vs.* RHE, followed by an identical experiment in O_2-saturated electrolyte.

The stability of the materials was investigated using a combination of step-cycles, the load-cycling (LC) protocol (10,000 square cycles; 0.6 – 1.0 V *vs.* RHE, 3s – 3s, in Ar- or O_2-saturated 0.1 M H_2SO_4 thermostated at T = 80°C or 60°C).

The nitrite adsorption method [35] was used to determine the active site density (SD) and the turnover frequency (TOF) of the materials. In order to stabilize the nitrite ions, an acetate buffer at pH 5.2 was used as the electrolyte. The catalyst loading was 0.3 mg cm^{-2}. After electrochemical break-in, characterization and ORR polarization curves, a nitrite containing solution (0.125 M of $NaNO_2$ in Milli-Q water) was used to poison the catalyst layer. The nitrite stripping was recorded in a potential range of 0.2 to - 0.2 V *vs.* RHE. The cyclic voltammograms and the ORR polarization curves were obtained before, during and after the nitrite poisoning. The SD, the TOF and the TOF' were calculated using the following equations:

$$\mathrm{SD\ (sites\ g^{-1})} = \frac{\mathrm{Q_{strip}(C\ g^{-1})} \times \mathrm{N_A(mol^{-1})}}{\mathrm{n_{strip}} \times \mathrm{F\ (C\ mol^{-1})}} \quad (1)$$

$$\mathrm{TOF\ (s^{-1})} = \frac{\mathrm{\Delta j_k\ (A\ g^{-1})}}{F\ (C\ \mathrm{mol^{-1}}) \times MSD\ (\mathrm{mol\ g^{-1}})} \quad (2)$$

$$\mathrm{TOF'\ (s^{-1})} = \frac{\mathrm{MA\ (A\ g^{-1})}}{F\ (C\ \mathrm{mol^{-1}}) \times MSD\ (\mathrm{mol\ g^{-1}})} \quad (3)$$

Where Q_{strip} and n_{strip} are the excess coulometric charge and the number of electrons associated with the stripping of one nitrite ligand per site, respectively; F and N_A are the Faraday and the Avogadro constants, respectively; Δj_k is the kinetic current difference before and after the nitrite poisoning; MSD is the active site density expressed by mol g^{-1} and MA is the mass activity measured at pH =1 using a catalyst loading of 300 μg cm^{-2}.

Transmission Electron Microscopy (TEM) and Energy Dispersive X-ray Spectroscopy (X-EDS)

To analyze the materials before and after the ASTs, a JEOL 2010 TEM microscopy operated at 200 kV with a resolution of 0.19 nm was used. X-EDS spectra were recorded

in at least 6 different regions of the TEM grid. The quantitative analyses were performed using the Fe *K* line and the *K*-factors provided by the JEOL software.

High-Angle Annular Dark-Field Scanning Transmission Electron Microscopy Imaging (HAADF-STEM)

HAADF-STEM images for Fe-HT_1 material, in Figure 5, were obtained using Nion UltraSTEM 200, equipped with C3/C5 aberration corrector. The instrument was operated at 60 kV to mitigate the beam damage. The convergence semi-angle was 38 mrad, while the inner and outer collection semi-angle of HAADF detector are 70 and 210 mrad, respectively.

Atom-resolved HAADF-STEM images for Fe-HT_2 material, in Figure 5, were obtained using a Cs-corrected NION USTEM-200 electron microscope. The experiments are performed at 60 kV to reduce the beam damage, and with a convergence semi-angle of 30 mrad and a HAADF collection angle of 80 to 200 mrad.

The Fe-N-C materials were deposited onto a gold TEM grid (300 mesh, Lacey Carbon; Agar Sc. UK), and at least 3 different carbon particles located in different regions of the TEM grid were imaged at both low and high magnifications to see the overall carbon structures and the Fe atom distributions. After the AST, the TEM grid was rinsed with MQ-grade water, dried in air, and transferred back for STEM analyses in the exactly same position.

X-Ray Diffraction

To investigate the carbon phase of the fresh catalysts, a X'Pert PRO MPD PANalytical diffractometer was used. The XRD was operated at 45 kV and 40 mA in Bragg-Brentano mode using Cu (K_a mean) radiation (λ = 1.5419 Å). The 2θ angles extended from 10 ° to 60 ° using 0.033 ° steps and a step-time of 9.4 s.

Raman Spectroscopy

Raman spectroscopy was used to analyze the carbon micro-structure of the materials before and after the ASTs. Measurements were performed using a Renishaw InVia instrument, in a backscattering configuration, with an excitation at 532 nm. A x50 objective

(NA=0.75) was used to focus and collect the incident and scattered radiations respectively. The spectral resolution was lower than *ca*. 1 cm^{-1}. The “line mode” of the spectrometer along with rather low incident power densities (about 5 mW) at the sample prevented excessive sample heating and/or degradation under the focused laser beam, while allowing getting an averaged information over a ~50 μm^2 area in a single exposure.

X-ray Photoelectron Spectroscopy

The XPS measurement was performed by Kratos AXIS Supra X-ray photoelectron spectrometer with a monochromatic Al Kα light source at the power of 225 W and 300 W for survey and high-resolution measurements respectively. The data were acquired with 100 ms dwell time, 0.1 eV / 1 eV step size, and 20 eV / 160 eV pass energy. All results are averaged by three spots for each sample and analyzed by CasaXPS with a 70 % Gaussian / 30 % Lorentzian line shape for composition analyses.

Nitrogen Adsorption Measurements

The catalyst surface area and pore structure are analyzed using a Micromeritics 3Flex Analyzer. Nitrogen sorption isotherm was collected at 77 K with low pressure dosing mode (5 cm^3/g). Surface area was calculated by Brunauer, Emmett and Teller (BET) method and pore size distribution was obtained using NLDFT model (Non-Local Density Functional Theory).

AUTHOR INFORMATION

Corresponding Authors

* E-mail address: (P. A.) plamen.atanassov@uci.edu

* E-mail address: (L. D.) laetitia.dubau@lepmi.grenoble-inp.fr

ASSOCIATED CONTENT

Supporting Information

The supporting information includes:

- Table S1. Carbon speciation extracted from XPS patterns;
- Table S2. Nitrogen speciation extracted from XPS patterns;

- Table S3. Mass activity towards the oxygen reduction reaction, active site density (SD) and turnover frequency (TOF) values of Fe-HT_2 catalyst before and after different load-cycling protocols;
- XRD patterns, Raman spectra and BET results for the fresh iron-based catalysts;
- CVs, RRDE polarization curves for the peroxide species quantification for Fe-HT_1 and Fe-HT_2;
- CVs, ORR polarization curves and Tafel plots for the SD and TOF determination of Fe-HT_1 and Fe-HT_2 using the nitrite adsorption/reduction method;
- CVs and ORR polarization curves before and after ASTs for Fe-HT_1 and Fe-HT_2 catalyst;
- TEM images of Fe-HT_2 catalyst before and after ASTs performed under Ar or O_2 atmosphere.

Conflict of Interest Statement

The authors declare that they have no known competing financial interests or personal relationships that could have appeared to influence the work reported in this paper.

ACKNOWLEDGEMENTS

This work was performed within the framework of the Centre of Excellence of Multifunctional Architectured Materials “CEMAM” n◦ ANR-10-LABX-44-01. It was funded by the French National Research Agency via the ANIMA (grant number ANR-19-CE05-0039) project.

The authors acknowledge financial support from the CNRS-CEA “METSA” French network (FR CNRS 3507) on the platform LPS-STEM.

REFERENCES

1. Jaouen, F.; Proietti, E.; Lefèvre, M.; Chenitz, R.; Dodelet, J. P.; Wu, G.; Chung, H. T.; Johnston, C. M.; Zelenay, P., Recent Advances in Non-Precious Metal Catalysis for Oxygen-Reduction Reaction in Polymer Electrolyte Fuel Cells. *Energy Environ. Sci.* **2011**, *4*, 114-130.
2. Lefèvre, M.; Proietti, E.; Jaouen, F.; Dodelet, J. P., Iron-Based Catalysts with Improved Oxygen Reduction Activity in Polymer Electrolyte Fuel Cells. *Science* **2009**, *324*, 71-74.
3. Gewirth, A. A.; Varnell, J. A.; DiAscro, A. M., Nonprecious Metal Catalysts for Oxygen Reduction in Heterogeneous Aqueous Systems. *Chem. Rev.* **2018**, *118*, 2313-2339.
4. Martinez, U.; Komini Babu, S.; Holby, E. F.; Chung, H. T.; Yin, X.; Zelenay, P., Progress in the Development of Fe-Based PGM-Free Electrocatalysts for the Oxygen Reduction Reaction. *Adv Mater.* **2019**, *0*, 1806545.
5. Kumar, K.; Gairola, P.; Lions, M.; Ranjbar-Sahraie, N.; Mermoux, M.; Dubau, L.; Zitolo, A.; Jaouen, F.; Maillard, F., Physical and Chemical Considerations for Improving Catalytic Activity and Stability of Non-Precious-Metal Oxygen Reduction Reaction Catalysts. *ACS Catal.* **2018**, *8*, 11264-11276.
6. Osmieri, L., Transition Metal–Nitrogen–Carbon (M–N–C) Catalysts for Oxygen Reduction Reaction. Insights on Synthesis and Performance in Polymer Electrolyte Fuel Cells. *ChemEngineering* **2019**, *3*, 16.
7. Kramm, U. I.; Lefèvre, M.; Larouche, N.; Schmeisser, D.; Dodelet, J. P., Correlations Between Mass Activity and Physicochemical Properties of Fe/N/C Catalysts for the ORR in PEM Fuel Cell via ^{57}Fe Mössbauer Spectroscopy and Other Techniques. *J. Am. Chem. Soc.* **2014**, *136*, 978-985.
8. Asset, T.; Atanassov, P., Iron-Nitrogen-Carbon Catalysts for Proton Exchange Membrane Fuel Cells. *Joule* **2020**, *4*, 33-44.
9. Kramm, U. I.; Abs-Wurmbach, I.; Herrmann-Geppert, I.; Radnik, J.; Fiechter, S.; Bogdanoff, P., Influence of the Electron-Density of Fe N_4 -Centers Towards the Catalytic Activity of Pyrolyzed FeTMPPCl-Based ORR-Electrocatalysts. *J. Electroch. Soc.* **2011**, *158*, B69-B78.

10. Koslowski, U. I.; Abs-Wurmbach, I.; Fiechter, S.; Bogdanoff, P., Nature of the Catalytic Centers of Porphyrin-Based Electrocatalysts for the ORR: A Correlation of Kinetic Current Density with the Site Density of Fe−N_4 Centers. *J Phys. Chem. C* **2008**, *112*, 15356-15366.

11. Kramm, U. I.; Herranz, J.; Larouche, N.; Arruda, T. M.; Lefèvre, M.; Jaouen, F.; Bogdanoff, P.; Fiechter, S.; Abs-Wurmbach, I.; Mukerjee, S.; Dodelet, J.-P., Structure of the Catalytic Sites in Fe/N/C-Catalysts for O_2-Reduction in PEM Fuel Cells. *Phys. Chem. Chem. Phys.* **2012**, *14*, 11673-11688.

12. Yarlagadda, V.; Carpenter, M. K.; Moylan, T. E.; Kukreja, R. S.; Koestner, R.; Gu, W.; Thompson, L.; Kongkanand, A., Boosting Fuel Cell Performance with Accessible Carbon Mesopores. *ACS Energy Lett.* **2018**, *3*, 618-621.

13. Yang, L.; Larouche, N.; Chenitz, R.; Zhang, G.; Lefèvre, M.; Dodelet, J. P., Activity, Performance, and Durability for the Reduction of Oxygen in PEM Fuel Cells, of Fe/N/C Electrocatalysts Obtained from the Pyrolysis of Metal-Organic-Framework and Iron Porphyrin Precursors. *Electrochim. Acta* **2015**, *159*, 184-197.

14. Artyushkova, K.; Serov, A.; Rojas-Carbonell, S.; Atanassov, P., Chemistry of Multitudinous Active Sites for Oxygen Reduction Reaction in Transition Metal–Nitrogen–Carbon Electrocatalysts. *J Phys. Chem. C* **2015**, *119*, 25917-25928.

15. Matanovic, I.; Artyushkova, K.; Atanassov, P., Understanding PGM-Free Catalysts by Linking Density Functional Theory Calculations and Structural Analysis: Perspectives and Challenges. *Curr. Opin. Electrochem.* **2018**, *9*, 137-144.

16. Ramaswamy, N.; Mukerjee, S., Influence of Inner- and Outer-Sphere Electron Transfer Mechanisms during Electrocatalysis of Oxygen Reduction in Alkaline Media. *J Phys. Chem. C* **2011**, *115*, 18015-18026.

17. Ferrandon, M.; Kropf, A. J.; Myers, D. J.; Artyushkova, K.; Kramm, U.; Bogdanoff, P.; Wu, G.; Johnston, C. M.; Zelenay, P., Multitechnique Characterization of a Polyaniline-Iron-Carbon Oxygen Reduction Catalyst. *J. Phys. Chem. C* **2012**, *116*, 16001-16013.

18. Wu, G.; Johnston, C. M.; MacK, N. H.; Artyushkova, K.; Ferrandon, M.; Nelson, M.; Lezama-Pacheco, J. S.; Conradson, S. D.; More, K. L.; Myers, D. J.; Zelenay, P., Synthesis-Structure-Performance Correlation for Polyaniline-Me-C Non-Precious Metal Cathode Catalysts for Oxygen Reduction in Fuel Cells. *J. Mater. Chem.* **2011**, *21*, 11392-11405.

19. Koslowski, U.; Herrmann, I.; Bogdanoff, P.; Barkschat, C.; Fiechter, S.; Iwata, N.; Takahashi, H.; Nishikori, H., Evaluation and Analysis of PEM-FC Performance using Non-Platinum Cathode Catalysts based on Pyrolysed Fe- and Co-Porphyrins - Influence of a Secondary Heat-treatment. *ECS Trans.* **2008**, *13*, 125-141.

20. Osmieri, L.; Monteverde Videla, A. H. A.; Specchia, S., Activity of Co–N Multi Walled Carbon Nanotubes Electrocatalysts for Oxygen Reduction Reaction in Acid Conditions. *J. Power Sources* **2015**, *278*, 296-307.

21. Domínguez, C.; Peña, M. A.; Rojas, S.; Pérez-Alonso, F. J., Effect of the Pyrolysis Atmosphere and Nature of Iron Precursor on the Structure and Activity of Fe/N Based Electrocatalysts for the Oxygen Reduction Reaction. *Int. J. Hydrogen Energy* **2016**, *41*, 22560-22569.

22. Workman, M. J.; Serov, A.; Tsui, L.-k.; Atanassov, P.; Artyushkova, K., Fe–N–C Catalyst Graphitic Layer Structure and Fuel Cell Performance. *ACS Energy Lett.* **2017**, *2*, 1489-1493.

23. Serov, A.; Workman, M. J.; Artyushkova, K.; Atanassov, P.; McCool, G.; McKinney, S.; Romero, H.; Halevi, B.; Stephenson, T., Highly Stable Precious Metal-free Cathode Catalyst for Fuel Cell Application. *J. Power Sources* **2016**, *327*, 557-564.

24. Chen, Y.; Gokhale, R.; Serov, A.; Artyushkova, K.; Atanassov, P., Novel Highly Active and Selective Fe-N-C Oxygen Reduction Electrocatalysts Derived from In-situ Polymerization Pyrolysis. *Nano Energy* **2017**, *38*, 201-209.

25. Kramm, U. I.; Herrmann-Geppert, I.; Bogdanoff, P.; Fiechter, S., Effect of an Ammonia Treatment on Structure, Composition, and Oxygen Reduction Reaction Activity of Fe–N–C Catalysts. *J Phys. Chem. C* **2011**, *115*, 23417-23427.

26. Jia, Q.; Ramaswamy, N.; Tylus, U.; Strickland, K.; Li, J.; Serov, A.; Artyushkova, K.; Atanassov, P.; Anibal, J.; Gumeci, C.; Barton, S. C.; Sougrati, M. T.; Jaouen, F.; Halevi, B.; Mukerjee, S., Spectroscopic Insights Into the Nature of Active Sites in Iron–Nitrogen–Carbon Electrocatalysts for Oxygen Reduction in Acid. *Nano Energy* **2016**, *29*, 65-82.

27. Serov, A.; Artyushkova, K.; Niangar, E.; Wang, C.; Dale, N.; Jaouen, F.; Sougrati, M. T.; Jia, Q.; Mukerjee, S.; Atanassov, P., Nano-Structured Non-Platinum Catalysts for Automotive Fuel Cell Application. *Nano Energy* **2015**, *16*, 293-300.

28. Li, J.; Sougrati, M.-T.; Zitolo, A.; Ablett, J.; Oguz, I. C.; Mineva, T.; Matanovic, I.; Atanassov, P.; Cicco, A. D.; Kumar, K.; Dubau, L.; Maillard, F.; Jaouen, F., Identification of

Durable and Non-Durable FeN_x Sites in Fe-N-C Materials for Proton Exchange Membrane Fuel Cells. *Nat. Catal.* **2020**, *just accepted*, DOI: 10.1038/s41929-020-00545-2.

29. Proietti, E.; Jaouen, F.; Lefèvre, M.; Larouche, N.; Tian, J.; Herranz, J.; Dodelet, J. P., Iron-Based Cathode Catalyst with Enhanced Power Density in Polymer Electrolyte Membrane Fuel Cells. *Nat. Commun.* **2011**, *2*, 416.

30. Li, J.; Jia, Q.; Mukerjee, S.; Sougrati, M.-T.; Drazic, G.; Zitolo, A.; Jaouen, F., The Challenge of Achieving a High Density of Fe-Based Active Sites in a Highly Graphitic Carbon Matrix. *Catalysts* **2019**, *9*, 144.

31. Santori, P. G.; Speck, F. D.; Li, J.; Zitolo, A.; Jia, Q.; Mukerjee, S.; Cherevko, S.; Jaouen, F., Effect of Pyrolysis Atmosphere and Electrolyte pH on the Oxygen Reduction Activity, Stability and Spectroscopic Signature of FeN_x Moieties in Fe-N-C Catalysts. *J. Electroch. Soc.* **2019**, *166*, F3311-F3320.

32. Zitolo, A.; Ranjbar-Sahraie, N.; Mineva, T.; Li, J.; Jia, Q.; Stamatin, S.; Harrington, G. F.; Lyth, S. M.; Krtil, P.; Mukerjee, S.; Fonda, E.; Jaouen, F., Identification of Catalytic Sites in Cobalt-Nitrogen-Carbon Materials for the Oxygen Reduction Reaction. *Nat. Commun.* **2017**, *8*, 957.

33. Strickland, K.; Miner, E.; Jia, Q.; Tylus, U.; Ramaswamy, N.; Liang, W.; Sougrati, M. T.; Jaouen, F.; Mukerjee, S., Highly Active Oxygen Reduction Non-Platinum Group Metal Electrocatalyst Without Direct Metal-Nitrogen Coordination. *Nat. Commun.* **2015**, *6*, 7343.

34. Artyushkova, K.; Matanovic, I.; Halevi, B.; Atanassov, P., Oxygen Binding to Active Sites of Fe–N–C ORR Electrocatalysts Observed by Ambient-Pressure XPS. *J Phys. Chem. C* **2017**, *121*, 2836-2843.

35. Malko, D.; Kucernak, A.; Lopes, T., *In situ* electrochemical quantification of active sites in Fe–N/C non-precious metal catalysts. *Nat. Commun.* **2016**, *7*, 13285.

36. Primbs, M.; Sun, Y.; Roy, A.; Malko, D.; Mehmood, A.; Sougrati, M.-T.; Blanchard, P.-Y.; Granozzi, G.; Kosmala, T.; Daniel, G.; Atanassov, P.; Sharman, J.; Durante, C.; Kucernak, A.; Jones, D.; Jaouen, F.; Strasser, P., Establishing Reactivity Descriptors for Platinum Group Metal (PGM)-Free Fe–N–C Catalysts for PEM Fuel Cells. *Energy Environ. Sci.* **2020**, *13*, 2480-2500.

37. Zitolo, A.; Goellner, V.; Armel, V.; Sougrati, M.-T.; Mineva, T.; Stievano, L.; Fonda, E.; Jaouen, F., Identification of Catalytic Sites for Oxygen Reduction in Iron- and Nitrogen-Doped Graphene Materials. *Nat. Mater.* **2015**, *14*, 937-942.

38. Charreteur, F.; Jaouen, F.; Dodelet, J. P., Iron Porphyrin-Based Cathode Catalysts for PEM Fuel Cells: Influence of Pyrolysis Gas on Activity and Stability. *Electrochim. Acta* **2009**, *54*, 6622-6630.

39. Martinaiou, I.; Shahraei, A.; Grimm, F.; Zhang, H.; Wittich, C.; Klemenz, S.; Dolique, S. J.; Kleebe, H. J.; Stark, R. W.; Kramm, U. I., Effect of Metal Species on the Stability of Me-N-C Catalysts During Accelerated Stress Tests Mimicking the Start-up and Shut-down Conditions. *Electrochim. Acta* **2017**, *243*, 183-196.

40. Chen, M.; He, Y.; Spendelow, J. S.; Wu, G., Atomically Dispersed Metal Catalysts for Oxygen Reduction. *ACS Energy Lett.* **2019**, *4*, 1619-1633.

41. Zhang, H.; Chung, H. T.; Cullen, D. A.; Wagner, S.; Kramm, U. I.; More, K. L.; Zelenay, P.; Wu, G., High-Performance Fuel Cell Cathodes Exclusively Containing Atomically Dispersed Iron Active Sites. *Energy Environ. Sci.* **2019**, *12*, 2548-2558.

42. Choi, C. H.; Baldizzone, C.; Grote, J. P.; Schuppert, A. K.; Jaouen, F.; Mayrhofer, K. J., Stability of Fe-N-C Catalysts in Acidic Medium Studied by Operando Spectroscopy. *Angew. Chem. Int. Ed.* **2015**, *54*, 12753-7.

43. Dubau, L.; Maillard , F., Unveiling the Crucial Role of Temperature on the Stability of Oxygen Reduction Reaction Electrocatalysts. *Electrochem. Commun.* **2016**, *63*, 65-69.

44. Kumar, K.; Dubau, L.; Mermoux, M.; Li, J.; Zitolo, A.; Nelayah, J.; Jaouen, F.; Maillard, F., On the Influence of Oxygen on the Degradation of Fe-N-C Catalysts. *Angew. Chem. Int. Ed.* **2020**, *59*, 3235-3243.